Subsurface imaging of fluvial deposits of the Wisła River valley in Kraków (southern Poland) by 2D ERT survey

Grzegorz BANIA[1, *] and Tomasz WOŹNIAK[2]

[1] AGH University of Science and Technology, Faculty of Geology, Geophysics and Environment Protection, Al. A. Mickiewicza 30, 30-059 Kraków, Poland

[2] Gołaśka 33, 30-619 Kraków, Poland

We describe the application of 2D ERT (electrical resistivity tomography) surveys to investigate the spatial complexity of fluvial deposits of the Wisła River valley in the eastern part of Kraków (southern Poland). All ERT survey lines were completed within the industrially influenced floodplain of the Wisła River at two research sites. Due to the transformation of the natural state of the environment through many years of industrial activity of the ArcelorMittal Kraków plant, some of the geomorphological elements analysed have been irretrievably transformed and hidden by anthropogenic accumulations such as waste landfills and engineering structures. Hence, many years of soil contamination have changed the primary resistivity characteristics of the subsurface. For this purpose, the measurement array applied combines standard arrays, i.e., Wenner-Schlumberger and Dipole-Dipole, which gave improved results (higher resolution) in comparison to the standard single array. The data interpretation method was supported by the calculation and visualization of the vertical and horizontal gradients of the interpreted resistivity within the resistivity sections. This approach allowed accurate determination of resistivity boundaries on the ERT resistivity sections and thus helped lithological interpretation of the fluvial deposits in the research area. The resistivity of water in a channel located within one of the analysed areas has impacted some of the research results. Furthermore, 2D ERT forward modeling was implemented to generate synthetic datasets. The synthetic data allowed investigation of the influence of groundwater contamination on the resistivity distribution within superficial layers, and also tested the ability of the 2D ERT model to recognize the detailed spatial distribution of palaeomeander (meander scar) infills. All methods have provided new information on the industrially influenced floodplain of the Wisła River in Kraków.

Key words: electrical resistivity tomography (ERT), gradients of interpreted resistivity, 2D ERT modeling, fluvial deposits, Wisła River valley, southern Poland.

INTRODUCTION

The area of the Wisła River in the Kraków area and its surroundings is an ideal site for a range of scientific studies. These include primarily geomorphological and geological research (e.g., Kalicki, 1991b, 2000; Starkel, 2001; Sokołowski, 2009 and references therein; Łajczak, 2021) as well as archaeological studies (e.g., Dobrzańska and Kalicki, 2015 and references therein; Mościcki et al., 2016; Łajczak and Zarychta, 2020).

Ground-penetrating radar (GPR; e.g., Vandenberghe and Van Overmeeren, 1999; Kostic and Aigner, 2007; Schrott and Sass, 2008; Słowik, 2011; Dara et al., 2019), electromagnetic induction (EMI; e.g., Conyers et al., 2008; De Smedt et al., 2011; Rejiba et al., 2018), and also electrical resistivity tomography (ERT; e.g., Baines et al., 2002; Giocoli et al., 2008; Chambers et al., 2012; Torrese et al., 2013; Rey et al., 2013; Matys Grygar et al., 2016; Bábek et al., 2018; Hošek et al., 2018; Akinbiyi et al., 2019) are effective non-invasive geophysical methods, widely used (in recent times) to investigate as well as determine the subsurface characterization of diverse deposits of fluvial origin. In particular, the latest geophysical method, i.e., ERT belonging to the direct current (DC) resistivity methods, is effective in the recognition of unconsolidated deposits due to the fact that they reveal significant variation in electrical resistivity. This depends primarily on the degree of porosity, the type of the medium filling the pore space (water or air) as well as on the mineralization of groundwater and the content of clay and sand (Telford et al., 1990).

Only a few regional surveys using geoelectrical methods on the Wisła River deposits in the Kraków area have so far been published. An integrated geological and geoelectrical analysis of the internal structure of a palaeomeander (meander scar) in Zabierzów Bocheński (~14 km E of the research site) was described by Kalicki and Mościcki (1997). These authors used 70

shallow boreholes, but also DC resistivity profiling and pen-etrometer-based resistivity profiling (PBRP) methods (for an explanation of the PBRP method, see e.g., Bania and Ćwiklik, 2014). Mościcki et al. (2014) published DC resistivity studies of the vicinity of the Wisła River flood bank in the village of Czernichów (~32 km W of the research site). The application of vertical electrical sounding (VES) and ERT methods together with shallow borehole data allowed quantitative assessment of the spatial distribution of various geoelectrical and geological layers. Furthermore, Mościcki et al. (2014) also referred to maps showing the top surfaces of the deposits investigated. Though not studying in detail the fluvial deposits of the Wisła River itself, Bania and Ćwiklik (2015) described subsurface zone conditions near an industrial waste heap with the use of the ERT method. Mościcki et al. (2016) interpreted the shallow geology of the area located in the manor and park in Branice with the use of VES, ERT as well as PBRP methods. This area is closest to (~0.5 km N of) the study area of this paper.

In this paper, we provide the results of 2D ERT surveys along with 2D ERT modeling applied to investigate the spatial distribution of alluvial deposits of the Wisła River valley, in the eastern part of the administrative boundaries of the city of Kraków and in the immediate vicinity of the ArcelorMittal Kraków plant. We also discuss aspects relevant to the potential local contamination of groundwater.

RESEARCH AREA

The Wisła River valley within the area investigated is in-cised into the deposits of the Carpathian Foredeep (Fig. 1A). The development of this tectonic unit has been associated with the Miocene evolution of the Outer Carpathians (Oszczypko, 2006; and references therein). The strata filling the Carpathian Foredeep comprise marine, fine-grained siliciclastic deposits of Miocene age, together with evaporites and tuffites (e.g., Oszczypko and Oszczypko-Clowes, 2012: fig. 5). These units, whose thickness in the Wisła River valley in the Kraków area varies from a few to several metres, lie directly on Upper Juras-sic and/or Upper Cretaceous deposits (Rutkowski, 1989; Wójcik and Lewandowski, 2010).

The Quaternary deposits that fill the Wisła River valley in the research area consist of gravels, gravels and sands, sands, silts, loams, peats and alluvial soils of Holocene age (see e.g., Rutkowski and Sokołowski, 1983; Rutkowski and Starkel, 1989; Rutkowski, 1993; Kalicki, 2000; Starkel, 2001 and references therein; Dobrzańska and Kalicki, 2015; also Fig. 2). There is also a view that these sands as well as gravels may date back to the Pleistocene (Rutkowski, 1993). In the gravels, quartz and sandstone clasts originating from the flysch deposits of the Outer Carpathians and/or from Upper Jurassic limestones to-gether with cherts, and to a lesser extent from Paleozoic lime-stones and Cretaceous sedimentary rocks have been identified petrographically (Kleczkowski, 1964; Mamakowa and Środoń, 1977; Rutkowski and Sokołowski, 1983; Rutkowski, 1993). Pre-served fragments of subfossil black oak trunks are also associ-ated with alluvial deposits of the Wisła River (Kalicki and Krąpiec, 1991, 1995; Krąpiec, 1998).

Radiocarbon and dendrochronological dating through the sedimentary succession across the Wisła floodplain between Kraków and Niepołomice (cf. e.g., Dobrzańska and Kalicki, 2015: fig. 4) indicate their age from Lateglacial to Subatlantic. In the immediate vicinity of the research fields F-1 and F-2 de-scribed here, precise ages have been established for: (i) the Kujawy sites – 440–560 AD and 900–1050AD (site 1); 1310–1320 AD (site 2); (ii) the Pleszów site – 13 260 ±160 BP;

(iii) the Branice site (that includes part of the F-1 research site) – 5190 ±70 BP; (iv) the Branice-Stryjów site – 2200 ±70 and 1480 ±60 BP as well as 1850 ±60 BP; and (v) for the Wyciąże site – 3785 ±60 BP and 415 ±50 BP (for site locations, see Fig. 2B).

The most characteristic features of the Lateglacial and Ho-locene floodplain of the Wisła River, the width of which is up to 7 km in the research area, are: (i) numerous sediment-filled palaeomeanders; (ii) oxbow lakes; and (iii) Young Pleniglacial and Lateglacial alluvial braidplains that functioned as backswamps during the Holocene (Fig. 2B).

Several of those morphological forms are no longer trace-able on the present-day floodplain of Wisła River, due to anthropogenic changes in the natural landscape. Next to the re-search sites F-1 and F-2 are industrial waste landfills, including the Pleszów post-industrial waste heap (PPIWH) (to the west of the research field F-1) and the Kujawy tailing ponds (KTP; to the north of the research site F-2; Figs. 1B and 2). These are re-lated to the activity of the ArcelorMittal Poland's Unit in Kraków – the historic Huta Sendzimira, positioned to the north-west of the map area shown in Figure 1. Slags and secondary wastes including moulding sands, and also post-industrial solid wastes, are stored on the PPIWH (Mikoś and Stewarski, 2003), while the KTP reservoirs (limited by earth embankments) are used for storing solid pollutants, such as ashes as well as slags and iron-bearing sludges (WIOŚ, 2012). Furthermore, a water-course flows through the research area F-1 towards the Wisła River, forming a channel of the industrial sewage system of the ArcerolMittal steelworks, referred as the Kanar (Fig. 2A). It car-ries all postproduction waste washed away by rainwater from various facilities of the ArcerolMittal steelworks as well as also in the past leachates from the Ruszcza heap (Operacz, 2009), located north of the area shown in Figure 1. The anthropogenic changes to the landscape of the floodplain also relate to the ex-ploitation of natural aggregates, such as sands and gravels (Bogacz et al., 2003; gp in Fig. 1). They have been exploited in the past, with some being worked until the present.

Towards the north, the Holocene floodplain is restricted by a terrace with Pleistocene loess at its surface, 2–3 km in width and with a height of up to 20 m above the mean river level in the Wisła River valley in the research area (Mamakowa and Środoń, 1977; Gębica, 2004; Wójcik and Lewandowski, 2010; Starkel et al., 2017). Landslides are locally associated with the escarpments of this terrace (Wójcik, 2015a, b).

METHODS

FIELD SURVEYS

The surveys were carried out at two research sites, F-1 and F-2 (Fig. 1B), along six electrical resistivity tomography (ERT) profiles (Fig. 2). An AGI SuperSting R8/IP 8 channel multielectrode resistivity metre (Fig. 3C), with 112 electrodes for all survey lines, was used.

Four ERT profiles (ERT-1–4), each 444 m long with an elec-trode spacing of $x = 4$ m, were established at the F-1 research site (Fig. 1B). As shown in Figures 2A and 3A, B, the N–S trending ERT-1, 2 survey lines were parallel to the Kanar chan-nel as well as to the accompanying embankments. The ERT-1 profile was located on the western side of the Kanar channel, and the remaining profiles (ERT-2–4) on the opposite (eastern) side. The ERT-3 profile was situated outside the embankment within an area ~2.5 m higher than the first two ERT profiles (Fig. 3B). The distance between the ERT-1 and ERT-2 survey lines was 20 m, and between ERT-2 and ERT-3 – 47 m. The
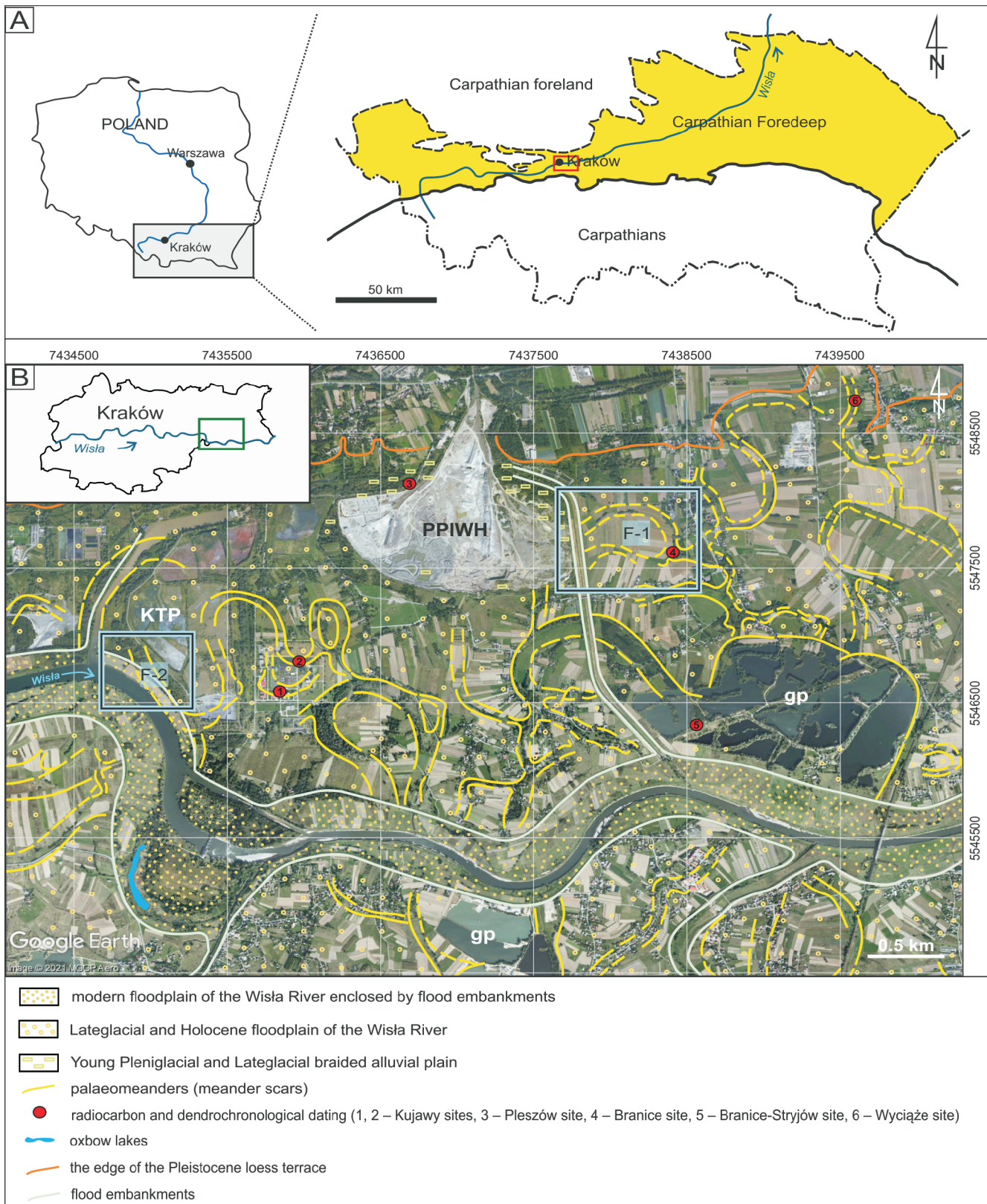
Fig. 1A – location of the research area (red rectangle) in the Polish sector of the Carpathian Foredeep; B – location of the F-1 and F-2 research sites (marked by blue rectangles) within its geomorphological setting (after Kalicki, 1991b, modified), overlaid on the Google Earth image of the Kraków area

PPIWH – Pleszów post-industrial waste heap, KTP – Kujawy tailing ponds, gp – gravel pits; coordinate system: Poland CS2000 zone 7
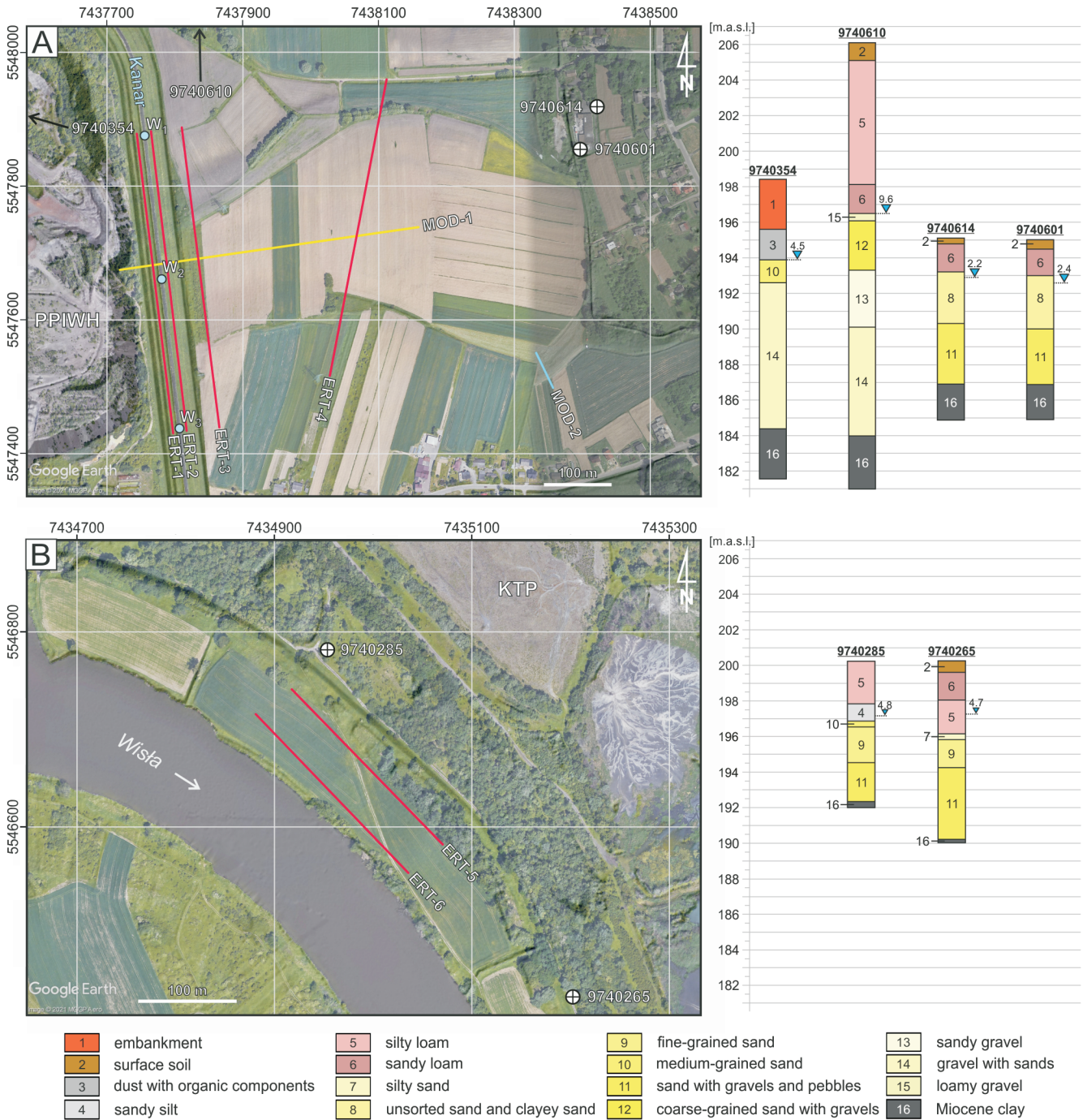
Fig. 2. Positions of the ERT survey lines, shallow boreholes and water resistivity measurement sites superimposed on a Google Earth image along with a DEM with 1 m cell size (source:www.geoportal.gov.pl)

Coordinate system: Poland CS2000 zone 7. The right side shows shallow borehole profiles with data obtained from the HYDRO Bank, Polish Geological Institute – National Research Institute. **A** – for the F-1 research site: W_1-W_3 – locations of water resistivity measurements. The 9740354 borehole is located approx. 735 m west of the W_1 point, while the 9740610 borehole is positioned around 410 m north of the W_1 point. Yellow line – synthetic 2D resistivity model MOD-1; blue line – geological cross-section and synthetic 2D resistivity model MOD-2. **B** – For the F-2 research site: the 9740285 and 9740265 boreholes are positioned on the first level of the KTP embankment (~3.5 m above the ERT-5, 6 survey lines)
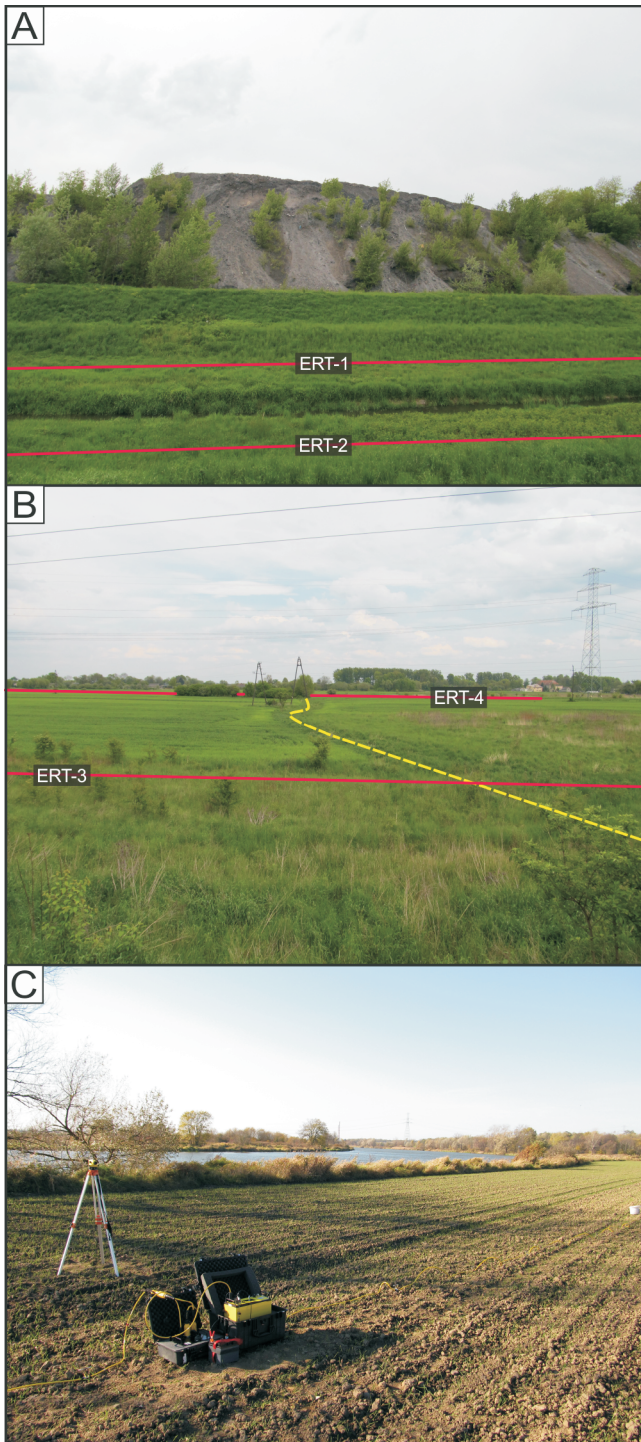
Fig. 3. Field views of the research sites

A – view showing the F-1 research site with the location of the ERT-1 and ERT-2 profiles. The Kanar channel is apparent among them. A post-industrial waste heap is in the background; **B** – general view of the F-1 research site in which the southern part of the palaeomeander (meander scar; yellow dashed line) crosses the ERT-3 and ERT-4 profiles; **C** – the photo depicts a view of the F-2 research site along with the ERT-6 profile and ERT equipment used for the field measurements. The Wisła River is in the background

ERT 4 profile ran through meadows and farmlands (Figs. 2A and 3B) at the same altitude level as the ERT-3 profile. The distance between the southern edges of the ERT-3 and ERT-4 profiles was 180 m, whereas their northern ends were 310 m apart from each other.

Two ERT profiles (ERT-5, 6), each 222 m long with an electrode spacing of x= 2 m, were established within the F-2 research site (Fig. 1B). The NW–SE trending, parallel ERT profiles were spaced 45 m apart (Figs. 2B and 3B). Because of natural obstacles, the beginning of ERT-6 profile was moved to the northwest by 7 m in relation to the beginning of the ERT-5 profile.

Due to the different spacing at the F-1 and F-2 research fields the vertical and horizontal resolution for field F-2 (with a 2 m spacing) is higher.

During the survey, geodetic measurements were also carried out using an optical level and a GPS receiver. The positions of the ERT profiles and sites of the water resistivity measurements were determined in the Poland CS2000 zone 7 coordinate system. In the ERT measurements, each electrode was leveled, and their heights recorded for each research site in separate, local height systems.

Field data sets were collected with a combination of three different arrays. Initially, for measurements on the ERT-3 profile, this combination consisted of a 10-level Wenner array, combined with the appropriate instructions for the Schlumberger array and the dipole-dipole array. Technically, for the Wenner array spacings 'a' = 1,2,3,4,5,6,8,10,12,15 x and for the dipole-dipole lengths of the current and potential dipoles 'a' = 1,2,3,4,5,6,7 x and the distances between these dipoles 'n' = 1,2,3,4,5,6,7,8 were applied. This measurement pattern resulted in 7266 data points (including 2446 points for the Wenner-Schlumberger array and 4820 points for the dipole-dipole array) using a set of 112 electrodes along a single survey line (Table 1). Unfortunately, for the largest dipole-dipole spacing, i.e., parameters 'a' = 7 x and 'n' = 7, 8, a relatively low signal level was observed. This may have been related to interference from the power line located near the ERT-3 profile. Therefore, the dataset obtained was properly filtered, i.e., the recorded negative values of apparent resistivity and values with errors resulting from the repeated measurement for the same set of four electrodes at the level of 2% and more were removed. For the remaining profiles, i.e., ERT-1,2,4,5,6, a modified measurement protocol was applied. It consisted of the Wenner-Schlumberger array with the same set of 'a' spacings, while the parameters of the dipole-dipole array were limited to 'a' = 1,2,3,4,5,6 x and 'n' = 1,2,3,4,5,6. The use of 112 electrodes on these ERT survey lines enabled us to obtain 5785 data points (including 2446 points for the Wenner-Schlumberger array and 3339 points for the dipole-dipole array; Table 1). Making the measurements along a single profile, with the time of completing a single pattern instruction of equal to ~1.2 s and its two repetitions, took ~3.5 h. The use of similar high-resolution combined arrays, with overlapping data levels (Loke, 2012), has been reported (cf. Stummer et al., 2004, Berge, 2014; Woźniak and Bania, 2019a, b).

ERT FIELD DATA PROCESSING AND INVERSION

The ERT measurement data was processed using some routines of the *Res2Dinv* software (ver. 3.59.118; *Geotomo Software*; Loke, 2012). First, procedures were applied to auto-

Characteristics of the measurements and inversion parameters for the ERT method

Research site	Surface ERT survey line	Electrode no.	Spacing, a [m]	Data points no.	Data points no. – after filtration	Iteration no.	Absolute error [%]
F-1	ERT-1	112	4	5785	5477	8	1.12
	ERT-2			5785	5377	8	1.25
	ERT-3			7266	6352	9	1.48
	ERT-4			5785	5748	8	1.40
F-2	ERT-5		2	5784	5772	9	0.96
	ERT-6			5785	5785	8	0.79

matically remove possible negative values of apparent resistivity with manual removal of a few (at most) apparent resistivity values clearly deviating from the others in a given data level (i.e., obtained along the survey line using the same array and with the same 'a' and 'n' parameters). Then, to take account of the terrain morphology in the inversion, information on the height of the electrodes on the particular profiles was added to the datasets. Failure to take this element into account may adversely influence the inversion results (Fox et al., 1980; Loke, 2000; Lu et al., 2015). The same set of inversion parameters as shown in Woźniak and Bania (2019a) has been applied in inversion in this research. The most important inversion parameter applied was to select robust (blocky, L1-norm) inversion, which as numerous published studies have shown (see e.g., Loke et al., 2003; Elwaseif and Slater, 2010; Danielsen and Dahlin, 2010; Gonzales Amaya et al., 2016; Woźniak et al., 2018) develops models with sharp boundaries.

After the inversion, in the ERT-1–5 datasets, additional data filtering based on the 'RMS error statistics' option at the cutoff error level of 20% was applied. Such filtering allows removal of data points with a relatively large difference between the calculated and measured apparent resistivity values. Due to this, it is possible to automatically filter data points affected by noise (Loke, 2012). However, with the very good quality of the data, the ERT-6 dataset did not require its use. After additional filtering, the inversion for ERT-1–5 data was performed again. Thus, the resulting interpreted resistivity sections (Figs. 4 and 5) contain very low absolute error values (<1.5%). Table 1 provides some information on ERT data inversion.

In addition, in *Surfer* software (*Golden Software*), the vertical and horizontal gradients of the interpreted resistivity distributions have been calculated for all ERT sections (coloured dotted lines in Figs. 4 and 5). In the resistivity section, these gradients define the boundaries at which the "transition" from the zone of relatively low to relatively high interpreted resistivity (or vice versa) is the most dynamic. These zones should be characterised by a relatively high resistivity contrast in relation to each other. Otherwise, such a gradient may not be identified reliably enough. The analysis based on these gradients is a very unusual approach to visualizing ERT data. However, it can be helpful in the contextual interpretation of geoelectrical research results (see e.g., Mościcki et al., 2014; Woźniak et al., 2018; Woźniak and Bania, 2019a).

WATER RESISTIVITY FIELD MEASUREMENTS

Within the F-1 research site (Fig. 1B), water resistivity and temperature were also measured at three selected locations along the Kanar channel (W_1, W_2, W_3 in Fig. 2A). They correspond to the beginning, middle part, and end of ERT-1–3 profiles. Measurements have been carried out using a self-constructed probe, termed the RT (R – resistivity, T – temperature), the *MiniSting* apparatus and the *METEX M-4650CR* multimeter. The RT probe has a four-electrode Wenner array with a spacing 'a' = 5 cm, mechanically secured and embedded in a special plastic tube. The electrodes are rings made of stainless steel. A single thermistor (NTC type) for temperature measurement is also mounted inside the probe. To determine its geometric coefficient, the probe has been calibrated in laboratory conditions. The advantage of using the constructed probe is the possibility of *in situ* measurements by placing it in any watercourse or even lowering it to the bottom of a river or lake (the only limitation is the length of the connecting cable – in our setup it was 20 m). The apparent resistance has been measured using the MiniSting apparatus, which was then converted into a resistivity value based on the geometric coefficient of the RT probe. The multimeter was applied to measure the resistance of the thermistor, which was then converted into a temperature value.

2D ERT MODELING

In order to examine resistivity changes in the subsurface sediments with increasing distance from the PPIWH to the east as well as to show certain restrictions regarding 2D ERT methods (in the context of detailed identification of fluvial deposits), two synthetic models have been developed (Figs. 8 and 9). In this paper, forward modeling has been implemented by *Res2Dmod* software (ver. 3.03.06; *Geotomo Software*) utilizing finite-element calculations (Silvester and Ferrari, 1996; Loke, 2012). In both models, measurement with the use of 112 electrodes has been simulated; however, the electrode spacing x = 4.0 m was used for the MOD-1 model (Fig. 8) and x = 0.5 m for the MOD-2 model (Fig. 9). The terrain morphology obtained on the basis of a high-resolution digital elevation model (DEM), i.e., a rectangular mesh with a mesh size of 1 m x 1 m (source: www.geoportal.gov.pl), was used during the 2D ERT forward modeling for each model. In the case of the MOD-1 model, the electrode heights were appropriately converted to the local elevation system used by the authors (compliant with the ERT-1–4 profiles), while for the MOD-2 model a separate, individual elevation system was created for more convenient analysis of the results.

The MOD-1 model (Fig. 8) has been developed on the basis of the field measurements along the ERT-1–4 profiles (Fig. 4). The hypothetical measurement line has been so drawn as to intersect the ERT-1–3 profiles over a distance of 250 m and ERT-4 over a distance of 210 m (Fig. 2A). The resistivity values as well as the thicknesses of individual layers, especially at the intersections of the hypothetical MOD-1 and ERT-1–4 profiles, were designated based on the field inverse model resistivity sections obtained (Fig. 4). These intersections are at the follow-
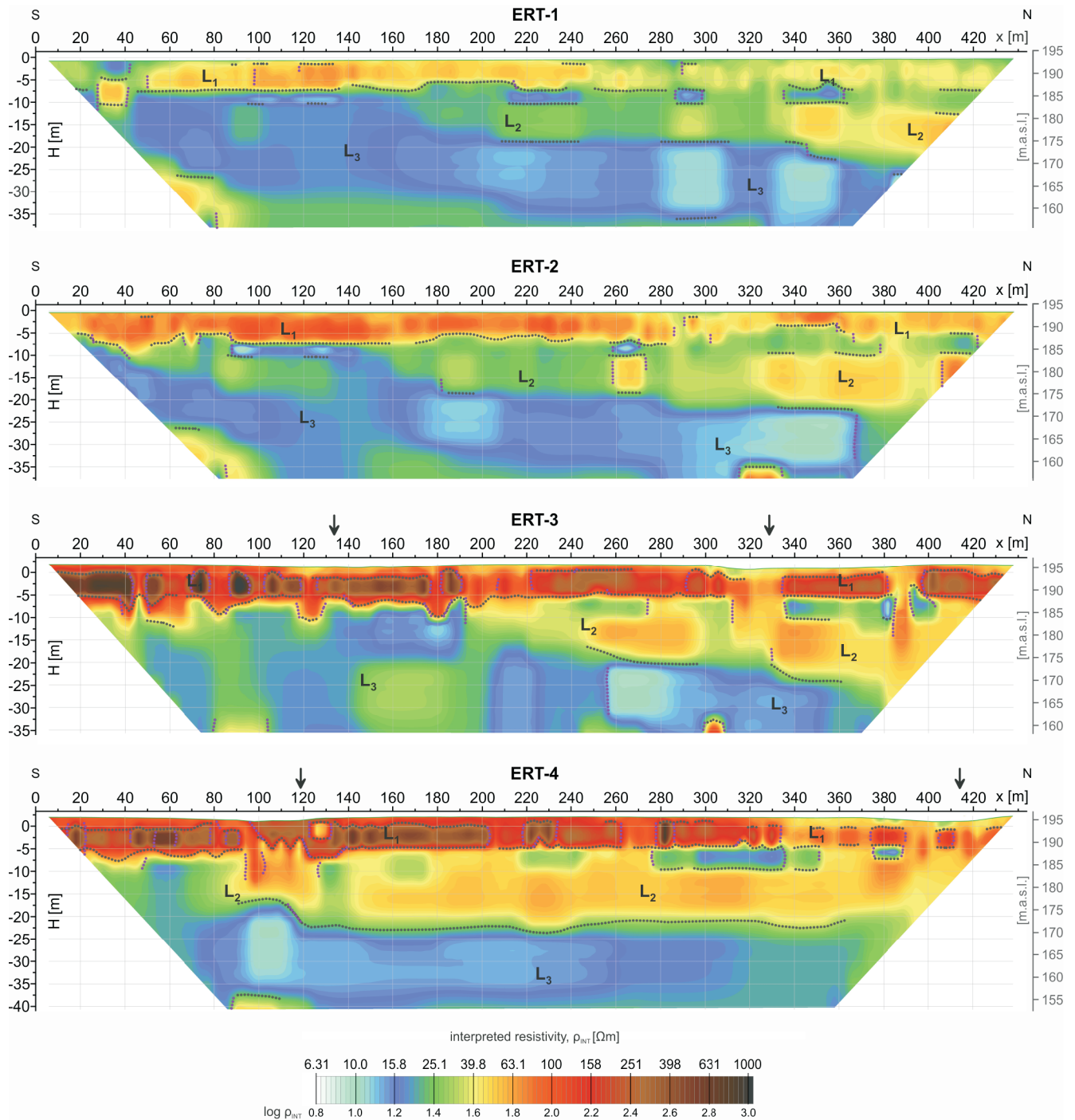
Fig. 4. ERT field data inversion results obtained from 2D surveys of the ERT-1–4 profiles with the calculated maximum values of the vertical (purple dotted lines) and horizontal (dark grey dotted lines) gradients of the interpreted resistivities

Some of the necessary data related to the inversion are included in Table 1; black arrows indicate distinct morphological depressions of the research area, found during the field measurements

ing distances: ERT-1 – 50 m; ERT-2 – 70 m; ERT-3 – 117 m and ERT-4 – 352 m. The MOD-1 model is intended to simulate the spread of pollutants (coming from the PPIWH and the Kanar channel) within the groundwater of the first and second modeled layers. The groundwater contamination is related to its mineralization and hence to its electrical resistivity (the higher the mineralization, the lower the resistivity; Dortman, 1992). Therefore, a high variability of resistivity values within these lay-

ers has been inferred. As shown in the MOD-1 model (Fig. 8A), the resistivities of the layers gradually increase eastwards, i.e., away from the PPIWH. The position of the MOD-1 profile line is marked in Figure 2A.

The MOD-2 model (Fig. 9) has been prepared on the basis of data derived by Kalicki (1991a). The main objective of the MOD-2 model was to explain the limited resolution of the results obtained when mapping the fluvial deposits. The sediment
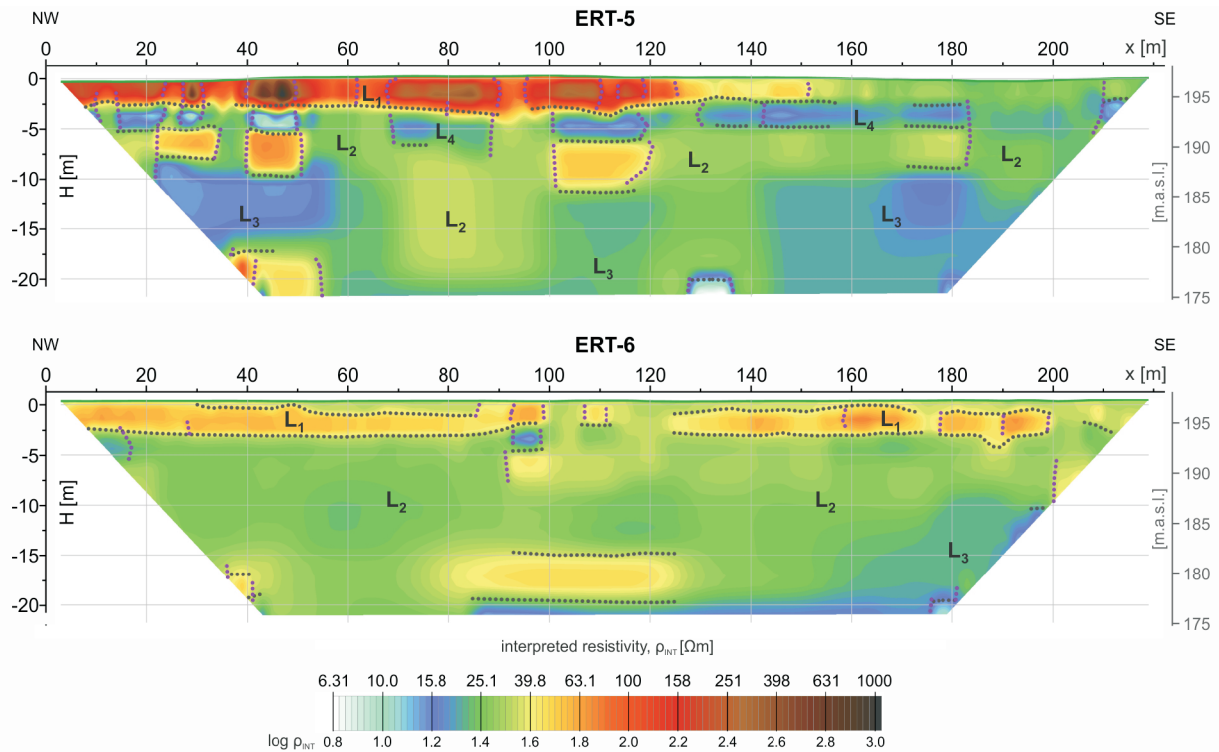
Fig. 5. ERT field data inversion results obtained from 2D surveys for the ERT-5–6 profiles with the calculated maximum values of the vertical (purple dotted lines) and horizontal (dark grey dotted lines) gradients of the interpreted resistivities

Some of the necessary data related to the inversion are included in Table 1. Black arrows indicate distinct morphological depressions of the research area, found during field measurements

resistivities within the MOD-2 model were selected arbitrarily on the basis of results obtained by the authors in association with studies conducted in Branice by Mościcki et al. (2016). The model is built of: 1 – sands, 140 m; 2 – silts, 30 m; 3 – sandy silts, 60 m; 4 – subfossil tree trunk, 200 m; 5 – silts and alluvial soils, 40 m (Fig. 9A). The position of the MOD-2 profile line is shown in Figure 2A.

Simulated measurement results for the synthetic resistivity models, given in this paper, have been calculated for the same array type as applied in the field. The synthetic data obtained were inverted using the same *Res2Dinv* inversion software (ver. 3.59.118; Geotomo Software) as used to process the ERT pseudosections measured in the field (with identical parameters).

RESULTS

The results of the ERT surveys for all profiles are shown in the form of two-dimensional sections of interpreted resistivity. They also feature the distributions of the vertical (dark grey dotted line) and horizontal (purple dotted line) gradients of the interpreted resistivity. ERT cross-sections for the F-1 research site are shown in Figure 4 and for the F-2 research site in Figure 5.

F-1 RESEARCH SITE FIELD DATA RESULTS

Within all cross-sections (ERT-1–4) at the F-1 research site (Fig. 4), three main geoelectric layers can be distinguished: L_1, L_2 and L_3. The L_1 subsurface layer is characterised by interpreted resistivity values ranging from ~40 to even 1000 m. In all sections, it extends along the entire length of the profiles and

shows relatively significant resistivity variation in places. In general, the mean interpreted resistivity of the L_1 layer increases from west to east, i.e., from the ERT-1 profile to the ERT-4 profile (Fig. 4). In the ERT-3 and ERT-4 sections, these values are similar. In the resistivity section for the ERT-1 profile, its average interpreted resistivity is ~50 m, for ERT-2 80 m, and for ERT-3 and ERT-4 200 m (Fig. 4). The bottom surface of this layer is undulating, especially in the ERT-3 and ERT-4 sections. This is particularly evident due to the gradients of the interpreted resistivity changes (Fig. 4). Regarding the variations in resistivity, similar observations can be made for the next deeper layer, L_2, but the values of the interpreted resistivity range here between 20 and 70 m. Its average resistivity for the ERT-1 cross-section is ~30 m, for ERT-2, 40 m, and for ERT-3 and ERT-4 it is 50 m (Fig. 4). Compared to the ERT-1–3 sections, in the ERT-4 cross-section it extends along almost the entire length, i.e., from ~70 m to the end of the profile, and its thickness remains similar at ~18 m. In the ERT-1–3 cross-sections, the L_2 layer is apparent from ~180 m of the profiles' length, where its thickness is relatively small. Gradually, towards the north it becomes thicker, reaching a thickness of up to 20 m at the ends of the sections. Its resistivity generally decreases towards the south. The ERT-4 section differs slightly from the others in terms of geoelectric structure (Fig. 4). As the ERT-4 profile was placed slightly farther than the ERT-1–3 group, its course is not parallel to them (Fig. 2A). Lastly, the L_3 layer is characterised in all sections by interpreted resistivity values in the range of ~10 to 30 m (Fig. 4). Within the ERT-1–3 sections, it is located at a distance from 0 to ~170 m, directly under the L_2 layer. On the other hand, in the ERT-4 section it borders with the L_2 layer at a shorter distance, i.e., from the beginning of the profile to its 75 m length.
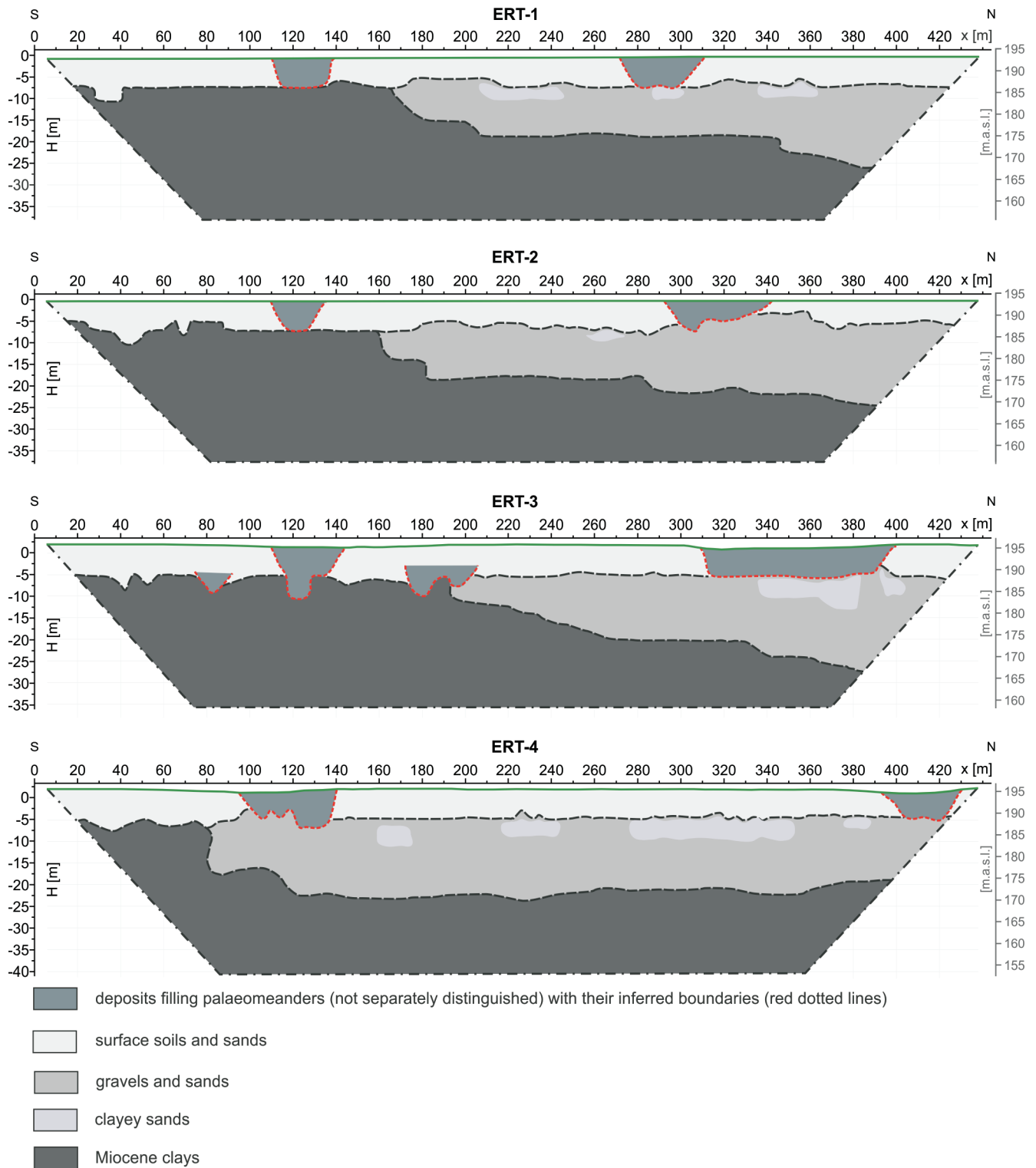
**Fig. 6. Hypothetical geological cross-sections through the floodplain of the Wisła River for the ERT-1–4 profiles
(F-1 research site)**

F-2 RESEARCH SITE FIELD DATA RESULTS

Four geoelectric layers have been distinguished in the ERT-5 and ERT-6 sections (Fig. 5). The L_1, L_2 and L_3 layers are present in both cross-sections, while layer L_4 was distinguished only in the ERT-5 section. The L_1 layer, which is nearest to the surface, is characterised by interpreted resistivity values ranging from ~30 to as high as 1000 m for the ERT-5 section and from ~30 to 70 m for the ERT-6 section (Fig. 5). This layer extends along the entire length of the ERT-6 section, while in the case of the ERT-5 section it gradually disappears to the east, being replaced by the low-resistivity (15–30 m) L_4 layer that extends to the surface. Within the L_4 layer there are zones with very low interpreted resistivity values of ~10 m. Several of these can be seen between ~20 to 50 m along the ERT-5 profile (Fig. 5). The L_2 layer with an interpreted resistivity of 30–60 m
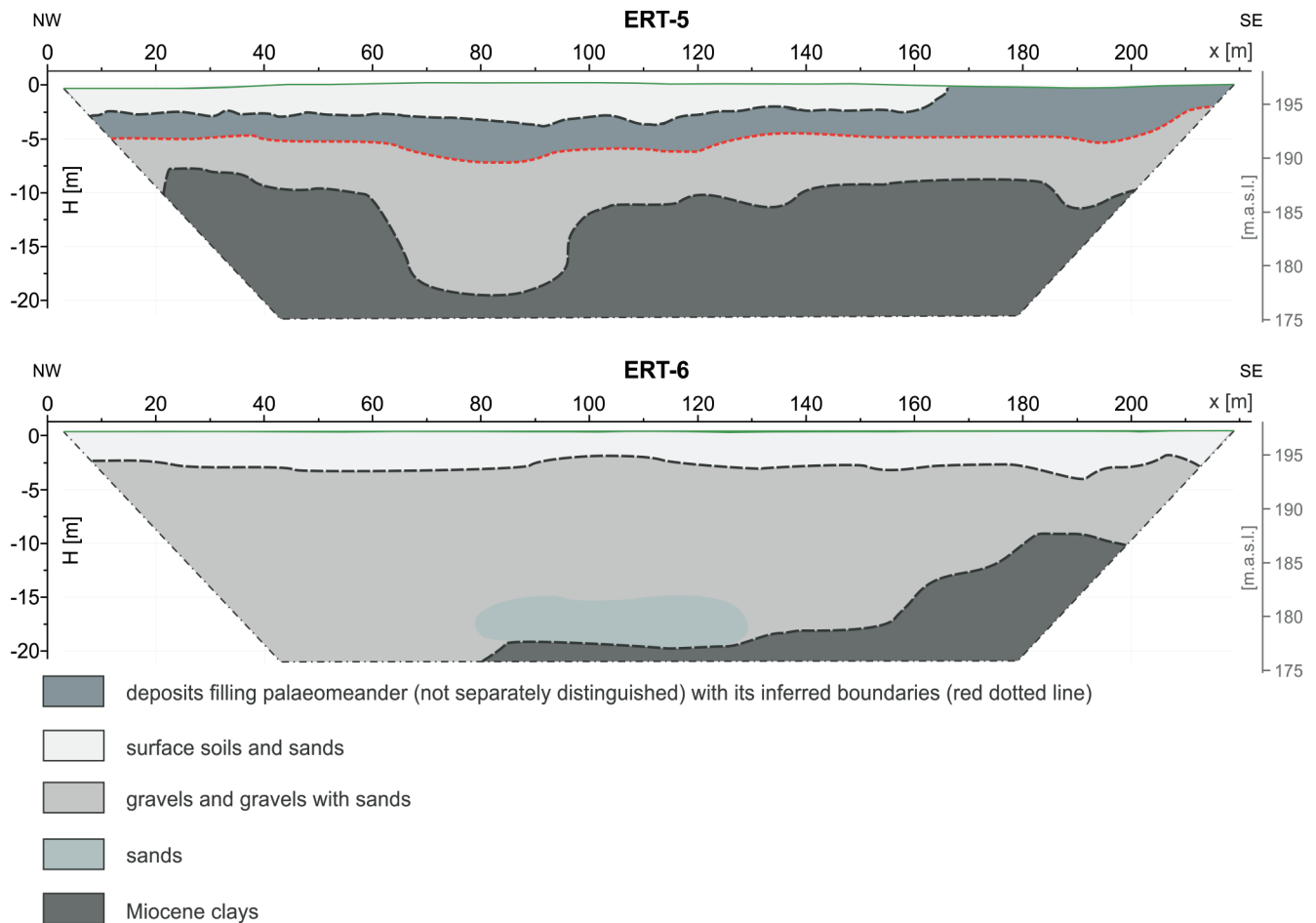
Fig. 7. Hypothetical geological cross-sections through the floodplain of the Wisła River for the ERT-5, 6 profiles (F-2 research site)

extends across the entire section, and between 70 and 100 m its thickness rapidly increases. In the geoelectric image, it also influences the complicated course of the top surface of the L_3 layer (~10–20 m). Two anomalous zones can be noticed within it. The first one (high-resistivity) is apparent in the lower left corner of the section, and the second one (low-resistivity) at a distance of ~130 m (Fig. 5). In the second cross-section (ERT-6), the L_2 layer dominates and is characterised by a slightly lower interpreted resistivity value than for the ERT-5 section. The L_3 layer is apparent at a length of ~80 m along the profile, at a depth of 20 m, and extends farther towards the east, where from ~150 m of the profile length it gradually becomes shallower.

WATER RESISTIVITY MEASUREMENT RESULTS

The results of the measurements of water resistivity within the Kanar channel (Fig. 2A) are as follows: (i) for the W_1 – resistivity: 3.44 m, temperature: 21.8°C; (ii) for the W_2 – resistivity 3.50 m, temperature: 21.9°C; and (iii) for the W_3 – resistivity: 3.75 m, temperature: 20.8°C.

DISCUSSION

RESISTIVITY/LITHOLOGY INTERPRETATION

Four geoelectrical layers (L_1, L_2, L_3, and L_4, respectively) have been distinguished in the inverse model resistivity sections (Figs. 4 and 5) based on the ERT results together with data originating from surrounding boreholes and including previous geological information. In order to better illustrate the interpretation results, inferred geological cross-sections have been made for all geoelectrical sections (F-1 research site – Fig. 6; F-2 research site – Fig. 7). Information necessary as context to the interpretation is also included in Figure 10.

Due to the application of a combination of several measurement arrays, the geoelectrical sections obtained are characterised by high resolution (cf. Stummer et al., 2004), that is reflected in the high resistivity contrast, and within the layers distinguished. However, the situation becomes complicated when we analyze the gradients of the interpreted resistivity on the ERT sections. These turned out to be particularly helpful in determining the presumed lithological boundaries within the allu-
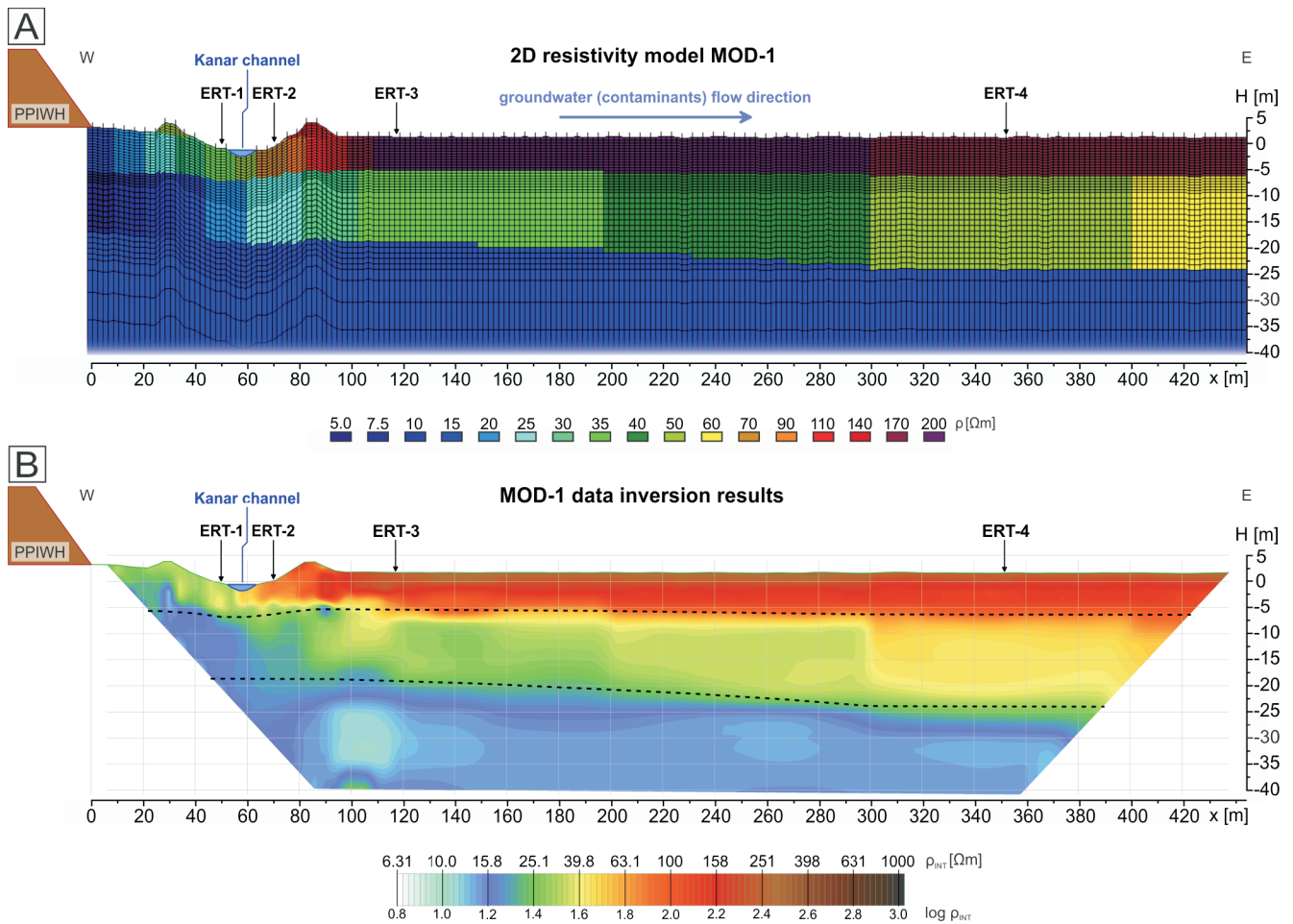
Fig. 8. Forward modeling procedure for the MOD-1 model

A – synthetic 2D resistivity model (for location see yellow line in Fig. 2A) based on the field data inversion results for ERT-1 to ERT-4 survey lines, PPIWH – Pleszów post-industrial waste heap; **B** – inversion result of forward model MOD-2 of the combined array, the dashed black lines in the figure emphasize the inferred positions of geological boundaries

vial deposits, because some of them are clearly defined by the resistivity gradients (Figs. 4 and 5). Nevertheless, because of the diverse geological structure of the research area, some of these boundaries, determined by the resistivity gradients, are locally broken. As shown in Figures 4 and 5, they also "blend" with much shorter boundaries, both vertical and horizontal, often creating envelopes for the smaller local zones, as is apparent within the individual layers.

Specific lithological units have been assigned to the geoelectrical L_1, L_2 and L_3 layers that are apparent within the F-1 research site on the ERT-1-4 sections (Fig. 6). The first of these (L_1) can be identified with surface soils and sands, together with the various deposits filling the palaeomeanders (not distinguished). It should be noted that due to the 4-metre electrode spacing (lower resolution within the near-surface zone), it was not possible to separate these individual lithological layers, so (apart from the deposits filling the palaeomeanders) they have been treated as one layer within the cross-sections (Fig. 6). The L_2 layer is probably built of gravels that locally pass (vertically and laterally) into gravels with sands as well as into clayey sands (cf. lower resistivity zones within the L_2 layer in Figs. 4 and 6). The Neogene sediments (more precisely Miocene clays) can be attributed to the deepest layer (L_3), the top surface of which is at various depths below ground level. The

shallowest part of this surface is positioned in the south, while its deeper part is situated in the north (Fig. 10A). Furthermore, the zones with a resistivity value of 30 m (green regions) apparent within the L_3 layer may be presumably linked with lithological changes in the Neogene clays (Rybicki et al. 2009; Mościcki et al., 2016).

As in the previous part of the interpretation, specific lithological units have been assigned to the geoelectrical L_1, L_2, L_3 and L_4 layers that are apparent within the F-2 research site in the ERT-5 to ERT-6 sections (Fig. 7). As the ERT-5, 6 profiles ran through farmland, the near-surface L_1 layer probably contains a thick zone of surface soils, mixed with sand deposits (Fig. 7). The next L_2 layer is probably built of gravels and gravels with sands. A distinct longitudinal zone apparent within the L_2 layer of the ERT-6 section, at between 80 and 130 m of its length (Fig. 5), with an increased interpreted resistivity value likely represents a local accumulation of sands (Fig. 7). The low-resistivity substrate (L_3) is represented by Miocene strata. Within the ERT-5 section, a distinct depression in the top surface of this layer (60-100 m of the profile length), is apparent (Fig. 7). In the case of the ERT-6 section, a comparable situation does not occur. In this context, it is also worth emphasising the complex course of the top surface of these deposits dips toward the Wisła River (Fig. 10B). The L_4 layer, apparent only in
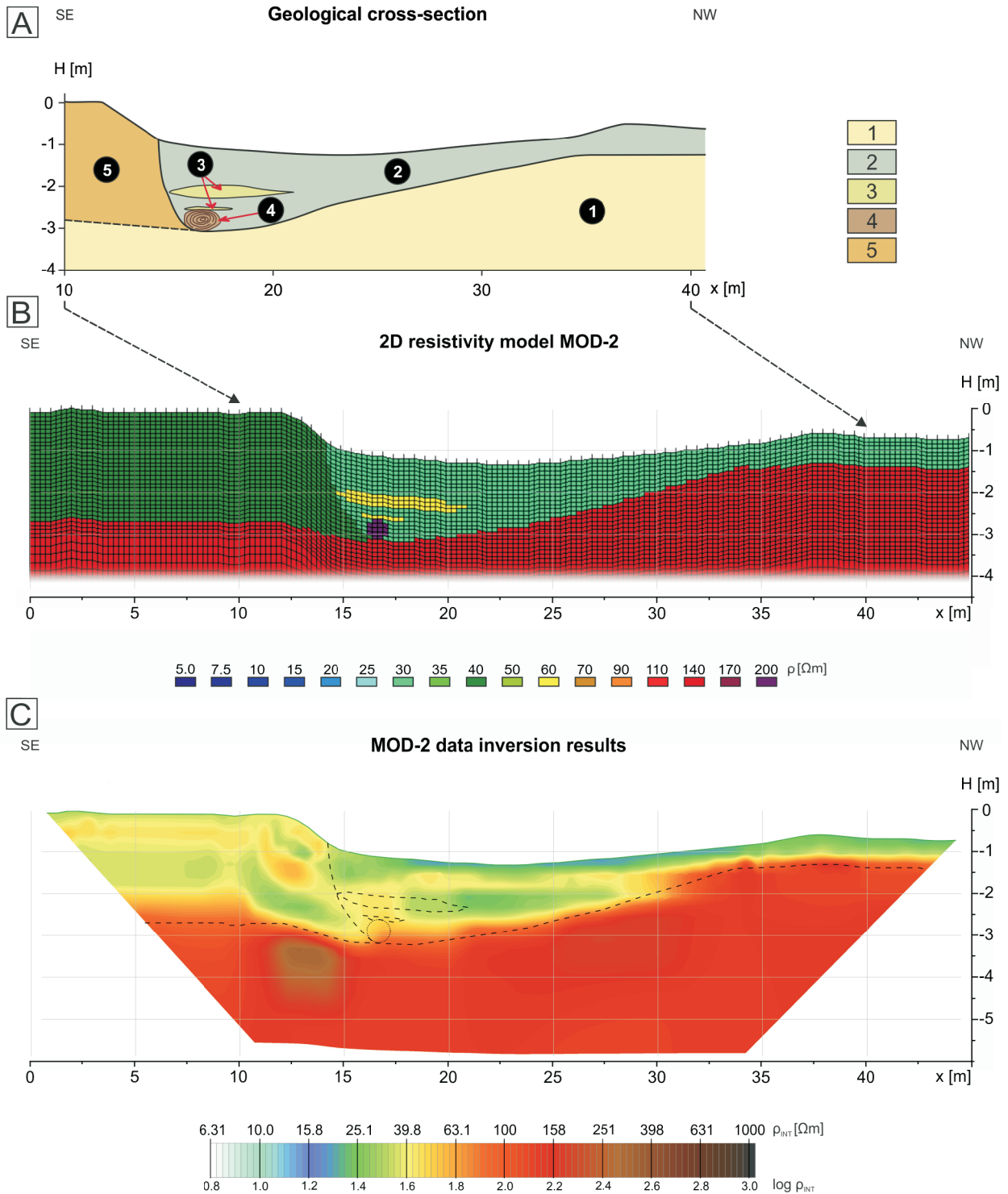
Fig. 9. Forward modeling procedure for the MOD-2 model

A – geological model (cross-section, for location see blue line in Fig. 2A) for resistivity 2D forward modeling (modified after Kalicki, 1999a): 1 – sands, 2 – silts, 3 – sandy silts, 4 – subfossil tree trunk, 5 – silts and alluvial soils; **B** – synthetic 2D resistivity model simulating the geological structure; **C** – inversion result of forward model MOD-2 of the combined array, the dashed black lines in the figure emphasize the positions of model-based geological boundaries

the ERT-5 section (Fig. 7), is most probably represented by the deposits filling the palaeomeander that has been recognized in this area (Kalicki, 1991b). The resistivities of this layer (Fig. 5) may indicate a high variability of these deposits, that can be presumably equated with different types of silts (sandy, clayey, organic).

Furthermore, several low-resistivity zones of ~10–15 m can be distinguished in the ERT-5 cross-section within the L_4

layer, at between 20 and 50 m of its length (Fig. 5). Their sharp boundaries are also emphasized by the gradients of the interpreted resistivity. Some of these zones are assumed to be artifacts related to the inversion process (see e.g., Loke and Barker, 1996; Bania and Ćwiklik, 2013) – effects accompanying the presence of a real, high-resistivity zone within the L_1 layer. These effects also continue within the L_2 layer in the ERT-5 section, where two zones of increased interpreted resistivity are ap-
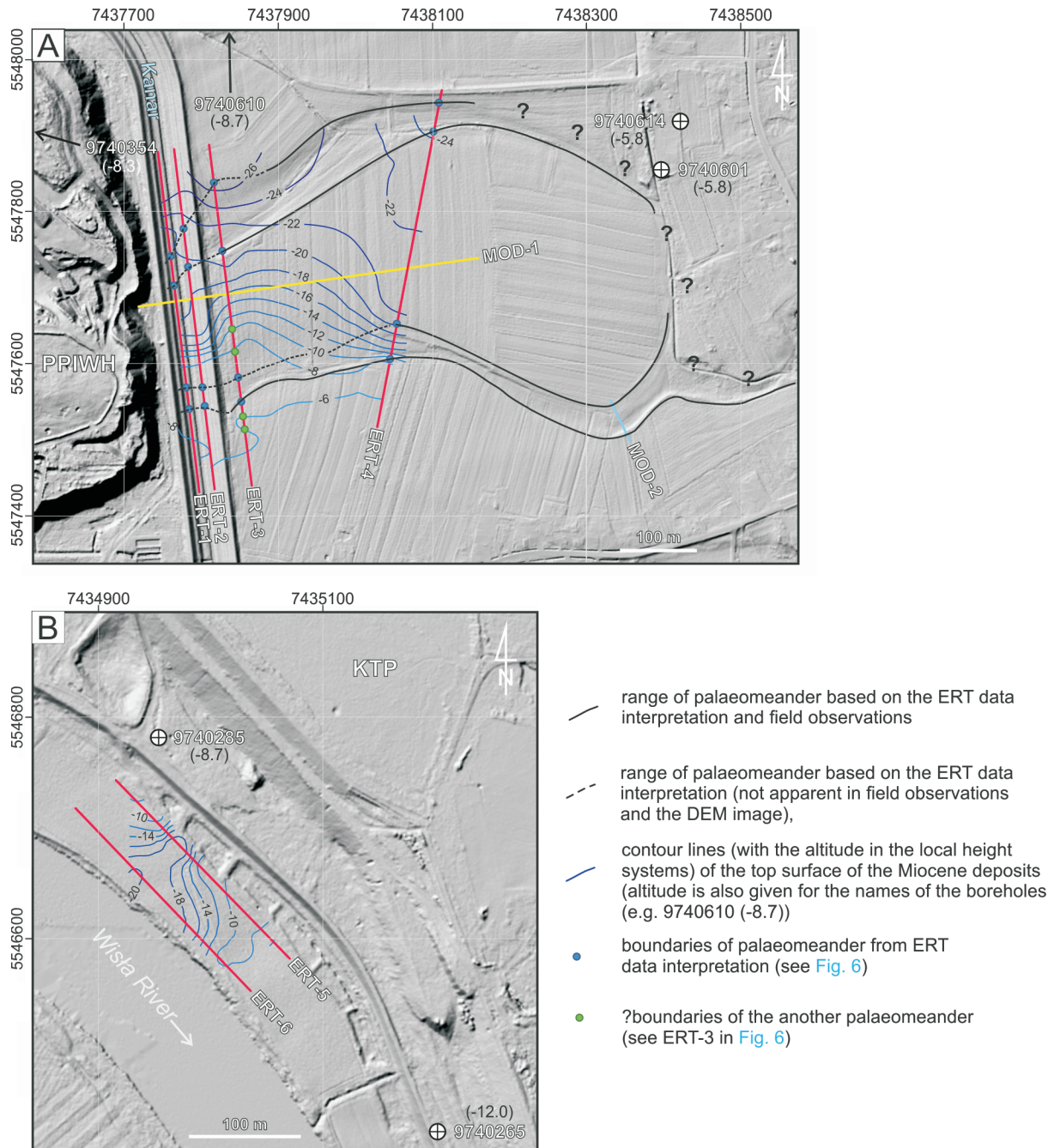
Fig. 10. Selected interpretation elements superimposed on the DEM image (with 1m cell size; source: www.geoportal.gov.pl), coordinate system: Poland CS2000 zone 7

A – for the F-1 research site; **B** – for the F-2 research site

parent, additionally separated by boundaries determined by marked gradients (Fig. 5). Their resistivity values may be related to inversion effects, although they may alternatively have geological origins (e.g., local accumulation of sands). Of the two deepest located zones in the ERT-5 cross-section (Fig. 5), the first is positioned in the lower left corner of this section and its interpreted resistivity value is ~40–100 m, while the second one is located at 130 m of its length (resistivity <10 m). These zones are presumably related to effects that locally occur (in some cases) on the edge blocks of the inversion grid as well as with the inversion process itself (Loke and Barker, 1996; Loke, 2012). Therefore, they should not be treated as real subsurface structures during interpretation. Similar zones can be indicated

on the other resistivity cross-sections, especially within their lower corners (see Figs. 4 and 5). Furthermore, it must be stressed in this context that ERT inverse model resistivity sections representing only a 2D approximation of the spatial geological structure (Loke and Barker, 1996).

THE IMPACT OF GROUNDWATER CONTAMINATION
ON THE GEOELECTRICAL CHARACTERISTICS
OF THE NEAR-SURFACE LAYERS

The unsealed Kanar channel contributes to the pollution of the aquifer in its nearest vicinity (Operacz, 2009), and has an impact on the resistivity values of the interpreted L_1 and L_2 layers in the geoelectrical sections (Fig. 4).

Previous research by Bania (2018), involving 2D/3D ERT forward modeling, has revealed that a contaminated medium will be characterised by significantly lower resistivity values, relative to a medium in which the groundwater is not contaminated. This research was based on the generalised lithological profile located close to the PPIWH and Kanar channel (Bania, 2018). Figure 1 of this paper (Bania, 2018) shows an assumed resistivity contrast of ~27:1 (medium with fresh water, = 80 m; contaminated medium, = 3 m). Moreover, two different scenarios for the boundary zones between fresh and contaminated groundwater were considered by this author. The first assumed a gradient where fresh and polluted waters slowly mix with each other, while the second was sharp, indicating rapid mixing of these waters, and thus a faster spread of pollutants within the aquifer (Bania, 2018).

As shown in our MOD-1 model (Fig. 8A), a smooth/gradational resistivity transition in the direction of the groundwater flow, with decrease in resistivity with increasing distance from the PPIWH, has been assumed. In the inverse model resistivity section (Fig. 8B), this phenomenon was well reflected. The highest pace of resistivity change is clearly apparent at the distance of up to 100 m (in the immediate vicinity of the PPIWH and Kanar channel). In the remaining section, the pace of change is noticeably slower. This, in turn, translates into significant resistivity variation (Fig. 8B). The MOD-1 model assumptions are coherent with the observations made analyzing the field inverse model resistivity sections ERT-1–4 (Fig. 4). Moving towards the east from the PPIWH, the resistivity values interpreted for these particular layers (first and second) increase (Fig. 4). This may be associated with the type of water mixing zone assumed in the MOD-1 model (Fig. 8A). Additionally, in the ERT-1 field cross-section (Fig. 4; located between the PPIWH and Kanar), the resistivity values interpreted are significantly lower than for the ERT-2 profile located on the opposite side of the Kanar channel. It follows that not only the Kanar channel contributes to the contamination of groundwater in this area, but also the PPIWH. Otherwise, i.e., if the PPIWH had no impact on the surrounding environment, the interpreted resistivities of the L_1 and L_2 layers in both ERT-1 and ERT-2 sections would be similar (Fig. 4).

The above interpretation is also supported by the observed slight decrease of water resistivity within the Kanar channel, and thus also an increase in its mineralization towards the south. The measured values of water resistivity converted into NaCl mineralization after Dortman (1992) are as follows: (i) 1.75 g/l NaCl for W_1; (ii) 1.65 g/l NaCl for W_2 and (iii) 1.60 g/l NaCl for W_3. Considering that the PPIWH is located next to the section of the Kanar channel (on which the water resistivity has been measured) that flows from north to south (Fig. 2A), the heap therefore has a noticeable negative impact on the hydrogeological environment in this area.

Due to the complex structure of the MOD-1 model (Fig. 8A) and the specific terrain morphology, the resistivity cross-section obtained by inversion (Fig. 8B) is not free from artifacts. Several are located over the distances of: (i) 30 m – a low-resistivity vertical zone; (ii) 90 m – a low-resistivity object on the boundary zone of the first and second layers; and (iii) 100 m – an object with a resistivity of ~25 m at the lower limit of the model (Fig. 8B).

Given the type of sediments deposited in the KTP, positioned close to the F-2 research site (Fig. 2B), it can be assumed that the hydrogeological environment there is also polluted. Duda et al. (2020), using the DC resistivity method, showed how large and problematic the scale of groundwater contamination in the vicinity of tailing ponds can be. However, in our interpretation, this issue does not have special importance. As shown in Figure 5, the interpreted resistivity values of the layers apparent in the ERT-5 and ERT-6 sections are similar. Fluctuations in the water table of the nearby Wisła River (Fig. 2B) also have a significant impact on the groundwater table. Thus, this may have an impact on seasonal changes in the interpreted resistivity values in the ERT cross-sections.

GEOMORPHOLOGICAL CONTEXT

The analysis of all data obtained provided an opportunity to trace the positions of the geomorphological forms, especially the palaeomeanders within both research fields.

The structure of the palaeomeander, cut by the ERT-3, 4 survey lines at the F-1 research site (Fig. 2A), is apparently marked in the field observations (Fig. 3B). The characteristic terrain depressions within the ERT-3, 4 sections are evident (black arrows in Fig. 4, see also Fig. 10) and indicate the lateral range of this structure within the F-1 research site. Based on the ERT results together with field observations, it can be inferred that the southern wing of this structure is positioned at between 110 and 140 m of the ERT-3 profile length, while the opposite wing is at between 310 and presumably even 400 m (Figs. 4 and 6). However, due to agricultural and industrial activities, their original boundaries may have been partially reshaped in the past (question marks in Fig. 10). The significant depression in the top surface of the sediments of the L_3 layer (up to the level of H = –10 m), within the southern wing may constitute its bottom surface (Figs. 4 and 6). This boundary correlates with the course of the interpreted resistivity gradients (Fig. 4). The lower part of this structure within its northern wing (310–335 m) is not as apparent as in its southern counterpart. This is demonstrated in the form of broken boundaries of the two courses of vertical gradients (Fig. 4). Presumably, the lower limit of the northern wing can be established at a depth of ~5–10 m below ground level (Fig. 6). The relatively large decrease in the resistivity of the interpreted geoelectrical L_1 layer is also characteristic of this site (Fig. 4). Another zone with a lower value of the interpreted resistivity, whose boundaries are determined by the broken gradients, is apparent from 380 to 400 m along the ERT-3 profile. Several characteristic structures at a depth of –5 to –10 m are also evident (one high-resistivity and two low-resistivity ones; Fig. 4). This phenomenon may be related to local lithological variation. The ERT-3 cross-section also shows two evident depressions in the top surface of the Miocene deposits (at 80 and 180 m of profile length; Fig. 4), similar to the depression indicated for the southern wing of the meander scar (Figs. 6 and 10A). Presumably, these structures, on the one hand, may be preserved parts of another palaeomeander associated with lateral displacement and migration of the river channel (Kalicki, 1991b, 2006). On the other hand, these may be local erosional structures. In the case of the ERT-4 section (Fig. 4), the boundaries of the palaeomeander are clearly defined on its southern side (90–135 m) and less apparent on the northern side (~370–430 m; Fig. 6). The southern wing is characterised by distinct denivelations in the top of the L_2 layer (marked also by the resistivity gradients) that specify its presumably lower limit (Fig. 4). For its northern wing, only local decreases in the resistivity values of the layers were observed, accompanied by numerous breaks in the course of the marked gradients of the interpreted resistivity. Because the area is anthropogenically transformed in the immediate vicinity of the ERT-1, 2 profiles (embankments of the Kanar channel, PPIWH; Fig. 2B), the elements of the palaeomeander are not apparent in the geoelectrical images. Based on the maps (Figs 1B and 2A) and ERT-1, 2 sections (Fig. 4), these forms are estimated to be located in similar places as indicated in the ERT-3 profile (Fig. 10A).

As can be seen on the map (Fig. 1B), the ERT-5, 6 profiles have been located within the area of the palaeomeander designated by Kalicki (1991b). The significant difference between the results obtained for the ERT-5 and ERT-6 cross-sections (Fig. 5) can mainly be ascribed to the ERT-6 profile being positioned on the border of or even outside the palaeomeander. Hence, the deposits filling this structure have not been distinguished in the hypothetical geological cross-section for that profile (Fig. 7).

It is evident from the data available from previous studies (Kalicki, 1991a, b; Kalicki and Mościcki, 1997) that filling of such structures can include several different sedimentary units. Kalicki (1991a) provided a topographic map as well as two different cross-sections (general and detailed) through the part of the palaeomeander within the F-1 research site. The attached figure shows the cross-section together with two sedimentary profiles at its edges (Kalicki, 1991a: fig. 13). However, their location is not clearly specified. In the next figure, based on four shallow boreholes, a geological cross-section of the internal structure of the southern wing of the palaeomeander was made (Kalicki, 1991a: fig. 14). The locations of these boreholes were not included on an additional topographic map attached to the same figure. The structure analysed is filled with silts, sandy silts and preserved tree trunk fragment of *Tilia* sp. (Kalicki, 1991a: figs. 13, 14).

The results we obtained from both F-1 and F-2 sites using the high-resolution ERT method did not, though, allow us to identify the specific lithologies that fill the palaeomeanders, and so these deposits have not been included in the lithological interpretation as separate units (Figs. 6 and 7). Using a smaller scale of measurements (smaller electrode spacing with the same high-resolution combination of measurement arrays), the possibilities of identifying individual sedimentary units are similar. When analyzing the inversion results for the MOD-2 model (Fig. 9C), there is relatively good distinction of the main lithologies, i.e. sands (140 m), silts (30 m) and alluvial soils (40 m; cf. Fig. 9B). Problems arise when trying to distinguish fine layers of sandy silt (60 m) and a subfossil tree trunk (200 m) within the silts (30 m). This is due to the small thicknesses of the sandy silt layers and the low resistivity contrast (2:1) between them and the surrounding silts (Fig. 9B). In the case of the tree trunk, the resistivity contrast with the surrounding layers is not much greater (in relation to the sandy substrate, the contrast is even lower). The trunk is also located at a relatively large depth compared to its size. This takes it beyond the range (resolution) of the ERT method. There is also a complicated morphology here, with the tree trunk being located near a lowering of the terrain. Despite the use of topography correction in the inversion process, it seems that this kind of morphology structure may additionally mask the presence of the tree trunk (see e.g., Tsourlos et al., 1999; Erdođan et al., 2008; Penz et al., 2013). The modeling performed shows that the results of ERT studies should be approached with caution. Some relatively small structures may not be distinguished in the section, because of a decrease in the resolution of the method with an increase in the depth range (Loke, 2012). Moreover, the more complicated the model, the more difficult it can be to reproduce it unambiguously. This is shown by the results of modeling stud-

ies by, e.g., Qarqori et al. (2012), Bania and Ćwiklik (2013), Bermejo et al. (2017), Woźniak and Bania (2019a).

CONCLUSIONS

1. High-resolution ERT method with the use of combined arrays allowed characterization of alluvial deposits of the Wisła River valley in the vicinity of Kraków. Several layers differing in resistivity have been distinguished in the inverse model resistivity sections. By correlating these results with the available borehole data, these layers were assigned to distinct lithological units.

2. Analysis of the gradients of the interpreted resistivity has allowed more precise recognition of the boundaries between different lithologies. In some cases, these boundaries determined by the gradients were not continuous due to the local geological structure of the research area. For some ERT profiles, by the application of gradient analysis, smaller local zones within the sedimentary units were also distinguished. These may reflect different lithologies or, in some cases, may result from the inversion process.

3. In the ERT cross-sections for the F-1 research site, increase in the interpreted resistivity of the near-surface geoelectrical layers to the east, i.e. away from the Pleszów post-industrial waste heap (PPIWH), has been observed. Additional analysis of water resistivity measurements in the Kanar channel showed that the PPIWH pollutes the water in the channel, as well as in the groundwater in the subsurface deposits. This trend comprises an increase in the interpreted resistivity values with distance from the source of contamination. 2D geoelectrical MOD-1 modelling together with corresponding inversion of the results illustrates this pattern more clearly.

4. Despite the use of high-resolution ERT with the use of combined arrays, we were not able to distinguish individual lithologies filling the palaeomeanders in the geoelectrical cross-sections. The ERT method provided a generalized image of the palaeomeander fill, as did 2D modeling (MOD-2) of part of a palaeomeander at the F-1 research site.

5. Data obtained from the ERT measurements at both the F-1 and F-2 research sites allowed the identification of the spatial distribution of lithologies within an area of the Wisła River valley in Kraków, providing a further implementation of the ERT method in fluvial deposits.

REFERENCES

Akinbiyi, O.A., Oladunjoye, M.A., Sanuade, O.A., Oyedeji, O., 2019. Geophysical characterization and hydraulic properties of unconsolidated floodplain aquifer system in Wamako area, Sokoto State, north-western Nigeria. Applied Water Science, **9**: 177.

Bábek, O., Sedláček, J., Novák, A., Létal, A., 2018. Electrical resistivity imaging of anastomosing river subsurface stratigraphy and possible controls of fluvial style change in a graben-like basin, Czech Republic. Geomorphology, **317**: 139–156.

Baines, D., Smith, D.G., Froese, D.G., Bauman, P., Nimeck, G., 2002. Electrical resistivity ground imaging (ERGI): a new tool for mapping the lithology and geometry of channel-belts and valley-fills. Sedimentology, **49**: 441–449.

Bania, G., 2018. ERT method in the study of chemical pollution of the hydrogeological environment – numerical analysis of 2D and 3D models. E3S Web of Conferences, **66**: 01007.

Bania, G., Ćwiklik, M., 2013. 2D Electrical Resistivity Tomography interpretation ambiguity – example of field studies supported with analogue and numerical modelling. Geology, Geophysics & Environment, **39**: 331–339.

Bania, G., Ćwiklik, M., 2014. Combined 2D Resistivity Imaging and Penetrometer-Based Resistivity Profiling – example of field studies. Conference Proceedings, 76th EAGE Conference and Exhibition 2014, Jun 2014, Volume 2014: 1–3.

Bania, G., Ćwiklik, M., 2015. Study of a Subsurface Zone Condition in the Vicinity of an Industrial Waste Heap with ERT Method. Conference Proceedings, 77th EAGE Conference and Exhibition 2015, Jun 2015, Volume 2015: 1–3.

Berge, M.A., 2014. Electrical resistivity tomography investigations on a paleoseismological trenching study. Journal of Applied Geophysics, **109**: 162–174.

Bermejo, L., Ortega, A.I., Guérin, R., Benito-Calvo, A., Pérez-González, A., Parés, J.M., Aracil, E., Bermúdez de Castro, J.M., Carbonell, E., 2017. 2D and 3D ERT imaging for identifying karst morphologies in the archaeological sites of Gran Dolina and Galería Complex (Sierra de Atapuerca, Burgos, Spain). Quaternary International, **433**: 393–401.

Bogacz, A., Poręba, E., Urbańska, A., Woliński, W., 2003. Mapa geośrodowiskowa Polski w skali 1:50 000, ark. Niepołomice (974) (in Polish). Państwowy Instytut Geologiczny, Warszawa.

Chambers, J.E., Wilkinson, P.B., Wardrop, D., Hameed, A., Hill, I., Jeffrey, C., Loke, M.H., Meldrum, P.I., Kuras, O., Cave, M., Gunn, D.A., 2012. Bedrock detection beneath river terrace deposits using three-dimensional electrical resistivity tomography. Geomorphology, **177–178**: 17–25.

Conyers, L.B., Ernenwein, E.G., Grealy, M., Lowe, K.M., 2008. Electromagnetic conductivity mapping for site prediction in meandering river floodplains. Archaeological Prospection, **15**: 81–91.

Danielsen, B.E., Dahlin, T., 2010. Numerical modelling of resolution and sensitivity of ERT in horizontal boreholes. Journal of Applied Geophysics, **70**: 245–254.

Dara, R., Kettridge, N., O. Rivett, M., Krause, S., Gomez-Ortiz, D., 2019. Identification of floodplain and riverbed sediment heterogeneity in a meandering UK lowland stream by ground penetrating radar. Journal of Applied Geophysics, **171**: 103863.

De Smedt, P., Van Meirvenne, M., Meerschman, E., Saey, T., Bats, M., Court-Picon, M., De Reu, J., Zwertvaegher, A., Antrop, M., Bourgeois, J., De Maeyer, P., A. Finke, P., Verniers, J., Crombé, P., 2011. Reconstructing palaeochannel morphology with a mobile multicoil electromagnetic induction sensor. Geomorphology, **130**: 136–141.

Dobrzańska, H., Kalicki, T., 2015. Morphology and land use of floodplains in the western part of Sandomierz Basin (southern Poland, Central Europe) in the Roman period. Quaternary International, **370**: 100–112.

Dortman, N.B., 1992. Petrophysics: Reference. In three books. Book one: Rocks and minerals. Nedra, Moscow.

Duda, R., Mżyk, S., Farbisz, J., Bania, G., 2020. Investigating the Pollution Range in Groundwater in the Vicinity of a Tailings Disposal Site with Vertical Electrical Soundings. Polish Journal of Environmental Studies, **29**: 101–110.

Elwaseif, M., Slater, L., 2010. Quantifying tomb geometries in resistivity images using watershed algorithms. Journal of Archaeological Science, **37**: 1424–1436.

Erdođan, E., Demirci, I., Candansayar, M.E., 2008. Incorporating topography into 2D resistivity modeling using finite-element and finite-difference approaches. Geophysics, **73**: F135–F142.

Fox, R.C., Hohmann, G.W., Killpack, T.J., Rijo, L., 1980. Topographic effects in resistivity and induced polarization surveys. Geophysics, **45**: 75–93.

Gębica, P., 2004. The course of fluvial accumulation during the upper Vistulian in Sandomierz basin (in Polish with English summary). Prace Geograficzne, **193**.

Giocoli, A., Magrě, C., Vannoli, P., Piscitelli, S., Rizzo, E., Siniscalchi, A., Burrato, P., Basso, C., Di Nocera, S., 2008. Electrical resistivity tomography investigations in the ufita Valley (southern Italy). Annals of Geophysics, **51**: 213–223.

Gonzales Amaya, A., Dahlin, T., Barmen, G., Rosberg, J-E., 2016. Electrical Resistivity Tomography and induced polarization for mapping the subsurface of alluvial fans: a case study in Punata (Bolivia). Geosciences, **6**: 51.

Hošek, M., Matys Grygar, T., Elznicová, J., Faměra, M., Popelka, J., Matkovič, J., Kiss, T., 2018. Geochemical mapping in polluted floodplains using in situ X-ray fluorescence analysis, geophysical imaging, and statistics: Surprising complexity of floodplain pollution hotspot. Catena, **171**: 632–644.

The HYDRO Bank (Polish Geological Institute – National Research Institute). https://www.pgi.gov.pl/psh/dane-hydrogeologiczne-psh/947-bazy-danych-hydrogeologiczne/9057-bankhydro.html

Kalicki, T., 1991a. Holocene generations of the Vistula paleomeanders near Cracow (in Polish with English summary). Kwartalnik AGH, Geologia, **17**: 25–66.

Kalicki, T., 1991b. The evolution of the Vistula river valley between Kraków and Niepołomice in late Vistulian and Holocene times. Geographical Studies, Special Issue, **6**: 11–37.

Kalicki, T., 2000. Grain size of the overbank deposits as carriers of paleogeographical information. Quaternary International, **72**: 107–114.

Kalicki, T., 2006. Reflection of climatic changes and human activity and their role in the Holocene evolution of Central European valleys (in Polish with English summary). Prace Geograficzne, **204**.

Kalicki, T., Krąpiec, M., 1991. Black oaks and Subatlantic alluvia of the Vistula in Branice-Stryjów near Cracow. Geographical Studies, Special Issue, **6**: 39–61.

Kalicki, T., Krąpiec, M., 1995. Problems of dating alluvium using buried subfossil tree trunks: lessons from the 'black oaks' of the Vistula Valley, Central Europe. The Holocene, **5**: 243–250.

Kalicki, T., Mościcki, W.J., 1997. Geological and geoelectrical study of alluvia at Vistula paleomeander in Zabierzów Bocheński (in Polish with English summary). Przegląd Geograficzny, **69**: 158–166.

Kleczkowski, A.S., 1964. Budowa geologiczna i wody gruntowe wysokiego tarasu Wisły na wschód od Krakowa (in Polish). Rocznik Polskiego Towarzystwa Geologicznego, **34**: 191–224.

Kostic, B., Aigner, T., 2007. Sedimentary architecture and 3D ground-penetrating radar analysis of gravelly meandering river deposits (Neckar Valley, SW Germany). Sedimentology, **54**: 789–808.

Krąpiec, M., 1998. Oak dendrochronology of the Neoholocen in Poland. Folia Quaternaria, **69**: 5–133.

Loke, M.H., 2000. Topographic modelling in resistivity imaging inversion. 62nd EAGE Conference & Technical Exhibition Extended Abstracts, D-2.

Loke, M.H., 2012. Tutorial: 2-D and 3-D Electrical Imaging Surveys. Geotomo Software, Malaysia.

Loke, M.H., Ackworth, I., Dahlin, T., 2003. A comparison of smooth and blocky inversion methods in 2D electrical imaging surveys. Exploration Geophysics, 34: 182–187.

Loke, M.H., Barker, R.D., 1996. Rapid least-squares inversion of apparent resistivity pseudosections by a quasi-Newton method. Geophysical Prospecting, 44: 131–152.

Lu, D.B., Zhou, Q.Y., Junejo, S.A., Xiao, A.L., 2015. A systematic study of topography effect of ERT based on 3-D modeling and inversion. Pure and Applied Geophysics, 172: 1531–1546.

Łajczak, A., 2021. Changes of the Vistula River channel pattern and overbank accumulation rate in the Carpathian Foreland (South Poland) under human impact. Studia Geomorphologica Carpatho-Balcanica, 55: 153–184.

Łajczak, A., Zarychta, R., 2020. Reconstruction of the morphology and hydrography of the centre of Kraków before the mid-13th century. Geographia Polonica, 93: 25–50.

Mamakowa, K., Środoń, A., 1977. On the Pleniglacial flora from Nowa Huta and Quaternary deposits of the Vistula Valley near Cracow (in Polish with English summary). Rocznik Polskiego Towarzystwa Geologicznego, 47: 485–511.

Matys Grygar, T., Elznicová, J., Tůmová, Š., Faměra, M., Balogh, M., Kiss, T., 2016. Floodplain architecture of an actively meandering river (the Ploučnice River, the Czech Republic) as revealed by the distribution of pollution and electrical resistivity tomography. Geomorphology, 254: 41–56.

Mikoś, T., Stewarski, E., 2003. Mining exploitations of the steelwork waste tips (in Polish with English summary). Warsztaty z cyklu „Zagrożenia naturalne w górnictwie", Materiały sympozjum: 435–451.

Mościcki, W.J., Bania, G., Ćwiklik, M., Borecka, A., 2014. DC resistivity studies of shallow geology in the vicinity of Vistula River flood bank in Czernichów village (near Krakow in Poland). Studia Geotechnica et Mechanica, 36: 63–70.

Mościcki, W.J., Bania, G., Ćwiklik, M., Florek-Odrazil, M., 2016. Budowa utworów przypowierzchniowych na terenie zespołu dworsko-parkowego w Branicach koło Krakowa – wyniki badań elektrooporowych (in Polish). In: Nawarstwienia historyczne miast Europy Środkowej (ed. M. Wardas): 407–423. Wydawnictwa AGH, Kraków.

Operacz, A., 2009. Rola gleby i strefy aeracji w procesach samooczyszczania się środowiska wód podziemnych zdegradowanych przez emisje przemysłowe w rejonie Huty Arcelor Mittal (in Polish). Ph.D. thesis, AGH University of Science and Technology, Kraków.

Oszczypko, N., 2006. Late Jurassic–Miocene evolution of the Outer Carpathian fold-and thrust belt and its foredeep basin (Western Carpathians, Poland). Geological Quarterly, 50 (1): 169–194.

Oszczypko, N., Oszczypko-Clowes, M., 2012. Stages of development in the Polish Carpathian Foredeep basin. Central European Journal of Geosciences, 4: 138–162.

Penz, S., Chauris, H., Donno, D., Mehl, C., 2013. Resistivity modelling with topography. Geophysical Journal International, 194: 1486–1497.

Qarqori, K., Rouai, M., Moreau, F., Saracco, G., Dauteuil, O., Hermitte, D., Boualoul, M., Le Carlier de Veslud, C., 2012. Geoelectrical tomography investigating and modeling of fractures network around Bittit Spring (Middle Atlas, Morocco). International Journal of Geophysics, 2012: 1–13.

Rejiba, F., Schamper, C., Chevalier, A., Deleplancque, B., Hovhannissian, G., Thiesson, J., Weill, P., 2018. Multiconfiguration electromagnetic induction survey for paleochannel internal structure imaging: a case study in the alluvial plain of the River Seine, France. Hydrology and Earth System Sciences, 22: 159–170.

Rey, J., Martínez, J., Hidalgo, M.C., 2013. Investigating fluvial features with electrical resistivity imaging and ground-penetrating radar: The Guadalquivir River terrace (Jaen, Southern Spain). Sedimentary Geology, 295: 27–37.

Rutkowski, J., 1989. Szczegółowa mapa geologiczna Polski w skali 1:50 000, ark. Kraków (973) (in Polish). Państwowy Instytut Geologiczny, Warszawa.

Rutkowski, J., 1993. Objaśnienia do Szczegółowej mapy geologicznej Polski w skali 1:50 000, ark. Kraków (973) (in Polish). Państwowy Instytut Geologiczny, Warszawa.

Rutkowski, J., Sokołowski, T., 1983. Preliminary petrographic study of Quaternary fluvial gravels of the Cracow region (south-ern Poland) (in Polish with English summary). Studia Geomorphologica Carpatho-Balcanica, 16: 99–108.

Rutkowski, J., Starkel, L., 1989. Influence of the human economy on geological processes in the Cracow region, south Poland (in Polish with English summary). Przegląd Geologiczny, 37: 312–319.

Rybicki, S., Krokoszyński, P., Herzig, J., 2009. Engineering-geological characteristic of the Krakow area subsoil, including historical deposits (in Polish with English summary). Kwartalnik AGH, Geologia, 35: 57–65.

Schrott, A., Sass, O., 2008. Application of field geophysics in geomorphology: advances and limitations exemplified by case studies. Geomorphology, 93: 55–73.

Silvester, P.P., Ferrari, R.L., 1996. Finite elements for electrical engineers (3rd ed.). Cambridge University Press.

Słowik, M., 2011. Reconstructing migration phases of meandering channels by means of ground-penetrating radar (GPR): the case of the Obra River, Poland. Journal of Soils and Sediments, 11: 1262.

Sokołowski, T., 2009. Topographic background of the settlement in Kraków (in Polish with English summary). Kwartalnik AGH, Geologia, 35: 67–76.

Starkel, L., 2001. Evolution of the Vistula River Valley Since the Last Glaciation till Present (in Polish with English summary). Instytut Geografii i Przestrzennego Zagospodarowania PAN, Warszawa.

Starkel, L., Michczyńska, D.J., Gębica, P., 2017. Reflection of climatic changes during interpleniglacial in the geoecosystems of South-Eastern Poland. Geochronometria, 44: 202–215.

Stummer, P., Maurer, H., Green, A.G., 2004. Experimental design. Electrical resistivity data sets that provide optimum subsurface information. Geophysics, 69: 120–139.

Telford, W.M., Geldart, L.P., Sheriff, R.E., 1990. Applied Geophysics. Cambridge University Press.

Torrese, P., Rainone, M.L., Colantonio, F., Signanini, P., 2013. Identification and investigation of shallow paleochannels in the chamelecon valley (Honduras): 1D vs 2D electrical resistivity surveys. Symposium on the Application of Geophysics to Engineering and Environmental Problems 2013: 321–331.

Tsourlos, P.I., Szymanski, J.E., Tsokas, G.N., 1999. The effect of terrain topography on commonly used resistivity arrays. Geophysics, 64: 1357–1363.

Vandenberghe, J., van Overmeeren, R.A., 1999. Ground penetrating radar images of selected fluvial deposits in the Netherlands. Sedimentary Geology, 128: 245–270.

Woźniak, T., Bania, G., 2019a. Analysis of the tectonic and sedimentary features of the southern margin of the Krzeszowice Graben in Southern Poland based on an integrated geoelectrical and geological studies. Journal of Applied Geophysics, 165: 60–76.

Woźniak, T., Bania, G., 2019b. Integrated geoelectrical and geological data sets for shallow structure characterization of the southern margin of the Krzeszowice Graben (Southern Poland). Data in Brief, 25: 104157.

Woźniak, T., Bania, G., Mościcki, W.J., Ćwiklik, M., 2018. Electrical resistivity tomography (ERT) and sedimentological analysis applied to investigation of Upper Jurassic limestones from the Krzeszowice Graben (Kraków Upland, southern Poland). Geological Quarterly, 62 (2): 287–302.

Wójcik, A., 2015a. Map of landslides and hazardous areas for mass movements at a scale of 1:10,000 for the Kraków city, Sheet M-34-65-C-c-2. Polish Geological Institute – National Research Institute.

Wójcik, A., 2015b. Map of landslides and hazardous areas for mass movements at a scale of 1:10,000 for the Kraków city, Sheet M-34-65-C-d-1. Polish Geological Institute – National Research Institute.

Wójcik, A., Lewandowski, J., 2010. Szczegółowa mapa geologiczna Polski w skali 1:50 000, ark. Niepołomice (974) (in Polish). Państwowy Instytut Geologiczny – Państwowy Instytut Badawczy, Warszawa.

WIOŚ, 2012. Raport o stanie środowiska w wojewdztwie małopolskim za rok 2011 (in Polish). Wojewódzki Inspektorat Ochrony Środowiska, Kraków.